






## Long-term volcano evolution controlled by lateral collapse at Antuco volcano, southern Andes, Chile

Jorge E. Romero <sup>1,2✉</sup>, Margherita Polacci <sup>1</sup>, Fabio Arzilli<sup>3</sup>, C. Ian Schipper<sup>4</sup>, Giuseppe La Spina <sup>5</sup>, Mike Burton <sup>1</sup>, Miguel A. Parada <sup>6</sup>, Juan Norambuena<sup>7</sup>, Alicia Guevara<sup>8</sup>, Sebastian Watt<sup>9</sup>, Hugo Moreno<sup>10</sup>, Luis Franco<sup>11</sup> & Jonathan Fellowes<sup>1</sup>

Beyond the catastrophic environmental effects of large (>1 km<sup>3</sup>) volcanic landslides, their impact on underlying magmatic systems remains unclear. Chemical variations in post-collapse volcanic products, alongside dramatic eruptive behaviour transitions reported from several volcanoes, imply that surface unloading directly influences subsurface magmatic processes. By combining petrologic data with magma ascent models, we track the post-collapse (<7 ka) magmatic system evolution of Antuco volcano (Chile). During the pre-collapse period, low-explosivity eruptions were sourced from a hotter and deeper storage region. However, the landslide-induced unloading and decompression reactivated a pre-existing, shallower, silicic magma reservoir, favouring more explosive activity. The pre-collapse conditions were restored after edifice regeneration over a few thousand years. Since shallow magma reservoirs are common beneath volcanoes (e.g. in Etna, Villarrica, or Fuji), similar responses could follow future lateral collapses. These findings are relevant when assessing volcanic hazards at gravitationally unstable or collapsed volcanoes on a hundred-to thousand-year timescale.

<sup>1</sup>Department of Earth and Environmental Sciences, University of Manchester, Manchester, UK. <sup>2</sup>Instituto de Ciencias de la Ingeniería, Universidad de O'Higgins, Rancagua, Chile. <sup>3</sup>School of Science and Technology, Geology Division, University of Camerino, Camerino, Italy. <sup>4</sup>School of Geography, Environment and Earth Sciences, Victoria University of Wellington, Wellington, New Zealand. <sup>5</sup>Istituto Nazionale di Geofisica e Vulcanologia, Osservatorio Etneo, Catania, Italy. <sup>6</sup>Departamento de Geología, Universidad de Chile, Santiago, Chile. <sup>7</sup>Independent researcher, Santiago, Chile. <sup>8</sup>Departamento de Metalurgia Extractiva, Escuela Politécnica Nacional, Quito, Ecuador. <sup>9</sup>School of Geography, Earth and Environmental Sciences, University of Birmingham, Birmingham, United Kingdom. <sup>10</sup>Independent researcher, Puerto Varas, Chile. <sup>11</sup>Observatorio Volcanológico de los Andes del Sur, Servicio Nacional de Geología y Minería, Temuco, Chile. ✉email: [jorge.romero@uoh.cl](mailto:jorge.romero@uoh.cl)

Volcanic lateral collapses, also called flank or sector collapses, are among the most destructive volcanic phenomena on Earth. Volcanoes are sites of inherent structural weakness driven by hydrothermal alteration, rapid growth, heterogeneous mechanical properties, continued magma intrusions and sub-volcanic basement spreading, all of which are factors contributing to flank instability and collapse<sup>1–3</sup>. These landslides involve unstable parts of a volcano<sup>4</sup> and produce rapid mass movements of incoherent and unsorted mixtures of rock and soil<sup>5</sup>. These debris avalanches can move faster than 100 m s<sup>-1</sup>, travel tens of kms from source, and inundate hundreds of square kilometres<sup>3,6</sup>. Debris avalanches have claimed hundreds of lives during the last century, with secondary phenomena (e.g. landslide-driven tsunamis) exacerbating these impacts<sup>7</sup>. At stratovolcanoes, lateral collapses are a ubiquitous but infrequent destructive process, shaping the development of volcanoes and forming part of long-term (i.e. thousands of years) cycles of volcano growth and collapse<sup>8</sup>.

Apart from the avalanches themselves, other immediate impacts of lateral collapses may involve quasi-instantaneous decompression of shallow magma plumbing systems and volcanic aquifers<sup>9</sup>, triggering violent lateral blasts that devastate the landscape with high dynamic pressures<sup>10</sup>. Rapid decompression may also destabilise the conduit, thus affecting subsequent eruptive activity<sup>11</sup>. Over a few to tens of thousands of years, lateral collapses may produce a variety of effects that influence the entire volcanic plumbing system because of unloading<sup>12–14</sup>. These changes include reconfiguration of shallow magma pathways and vent relocation<sup>15–20</sup>. Changes in the chemical composition and eruptive behaviour have also been reported because of upper-crustal reservoir disruption<sup>14</sup>. However, testing these relationships is challenging due to the difficulties in reconstructing a detailed eruptive chronology at individual volcanoes, which is needed to determine the role of edifice destruction and regrowth in controlling magma system evolution. As a result of this, the long-term consequences of lateral collapses are usually not systematically considered in hazard evaluation<sup>7,21</sup>, despite being a potentially important control on volcano behaviour, mainly due to the limited knowledge of how edifice collapse and regrowth influences volcano development<sup>18</sup>. There is thus a need for high-resolution eruption records to be combined with petrological studies and numerical approaches<sup>22</sup>, to better constrain the consequences of lateral collapses on volcano development. We have identified Antuco volcano, Chile, as the ideal site to investigate this topic.

Antuco is a stratovolcano of the southern Andes (Chile) that experienced a catastrophic lateral collapse at 6.9–7.2 ka BP. The collapse removed nearly 1 km of the cone height and transported a 6.4 km<sup>3</sup> debris avalanche that infilled a glacial valley towards the west, and its age was determined from a small brush branch dated by radiocarbon at the base of the deposit<sup>23</sup>. The volcano was previously thought to have erupted only basaltic lavas (51–54 wt.% SiO<sub>2</sub>) during its post-glacial (<17 ka) evolution<sup>24,25</sup>. However, recent evidence has reported andesites (61–62 wt.% SiO<sub>2</sub>) explosively erupted at around 4 ka BP<sup>26</sup>, as well as “compositionally anomalous” andesitic lavas<sup>14</sup> (~58 wt.% SiO<sub>2</sub>) nearly 3.4 ka ago<sup>22</sup>.

To understand how magma storage systems react to unloading by a lateral collapse, ideally at timescales of thousands of years, we need to investigate the eruptive products from before, during, and after a collapse. Several studies have been carried out on collapsed volcanic islands<sup>17,27,28</sup> or over decade-long timescales at continental volcanoes<sup>29–31</sup>. These studies report compositional changes during the post-collapse stage but typically based on limited geochronologic or compositional data. Here, we utilise stratigraphically sampled lavas and pyroclasts of Antuco volcano

representing the last 17 ka of activity to characterise their chemical, mineralogical and textural properties. This evidence is exploited to reveal the architecture and storage conditions within the magma system and to explain the variations in the volcanic activity after the lateral collapse. Finally, we use a numerical model of magma ascent to simulate the most likely magmatic conditions within the volcanic conduit during the collapse, to explore the immediate reaction of the system to unloading.

## Results

### Geology and location of the pre- and post-collapse products.

The eruption products described in this work are indicated in Supplementary Data 1. From its inception at ~150 ka up until 17 ka, lavas at Antuco span a wide compositional range from basalts to dacites (50.9–64.5 wt% SiO<sub>2</sub>); these products were likely sourced from a magma reservoir located 2–5 km below the old summit<sup>24</sup>. However, limitations of exposure prevent us exploring detailed trends in this stage of the volcano’s history. From 17 ka up until the collapse at 6.9–7.2 ka<sup>24</sup>, Antuco erupted exclusively basalts that formed blocky, ‘a’ā or rarely pahoehoe porphyritic lava flow morphologies. These produced flows with heights up to 30 metres. Many of them display lava tubes in the lower flanks of the edifice, exposing caves several metres in height. These lavas were cut by the collapse scar, so were presumably sourced from the original summit vent of the old Antuco edifice. This unit has been named “Late Antuco”<sup>24</sup> and we collected five samples from three different lavas stratigraphically spanning the lowermost, middle, and uppermost parts of the sequence.

We divide the post-collapse stage into an early and late post-collapse period. During the early post-collapse period, andesitic lavas reached 10 km west from the current summit, forming flow units up to 8 m thick and developing notable columnar jointing. Their maximum age is 3.4 ka, determined from charcoal found in an underlying paleosol<sup>23</sup>. We obtained fifteen new samples from these lava flows and three additional samples from pyroclastic units from the post-collapse sequence that are complemented with thirteen published data in Romero et al.<sup>26</sup>. The subsequent lavas of the late post-collapse stage (<3 ka) are also distributed west from the collapsed volcano and form the youngest edifice of Antuco; they correspond to ‘a’ā porphyritic basalts sourced from the summit cone or lateral fissures in the main cone (Fig. 1), with flow lengths up to 7 km and regular widths of 10–60 m. We obtained nine lava samples from these younger units for this study.

Two tephra samples (units β and δ) were collected from the bottom of the pyroclastic sequence east of Antuco (Fig. 2). They are reinterpreted as corresponding to the Late Antuco stage, rather than the post-collapse period, based on field observations that indicate a few thousand years gap between these tephra and overlying units<sup>23</sup>. Pyroclastic rocks associated with the post-collapse stage (early and late) are easily recognised on the flanks of both the collapsed and regenerated edifices. Wind-controlled dispersal led to preservation of air-fall scoria and pumice deposits mostly towards the east. The early post-collapse deposits with available geochemistry in the literature are (from older to younger) units ε and El Pino tephra (EPT; Fig. 2) (3.7–4.3 ka; ref. 26) and these samples (8) are further studied in this contribution. At 10 km to the west of Antuco, the deposits of dilute pyroclastic density currents (PDCs) directly overlie the debris avalanche deposit and underlie the early post-collapse lavas and their minimum age obtained from charcoal fragments in the uppermost exposures is 3.6 ka<sup>23</sup>. These deposits are exposed in the Laja river valley walls and reach a maximum thickness of 5 m; internally, they contain a fine-to-coarse ash matrix and beds of 20–30 cm thickness of abundant lapilli fragments, as well as cm-thick fine ash beds with

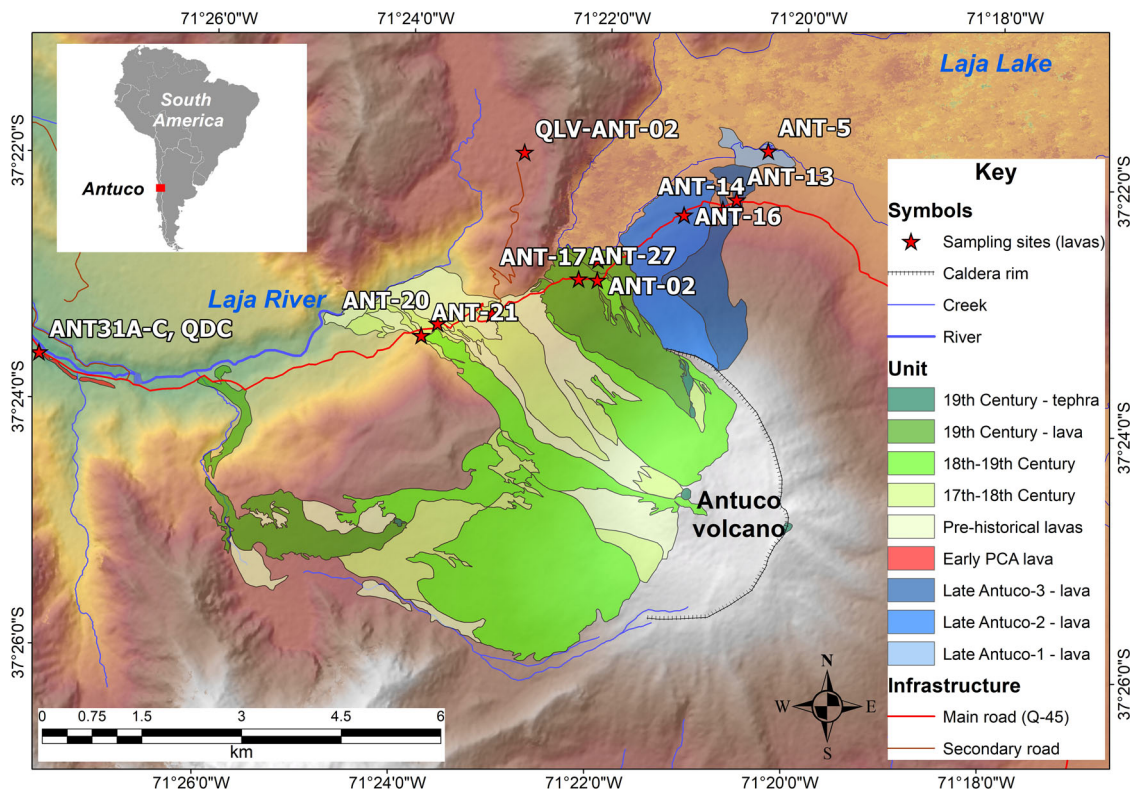


**Fig. 1** Map showing the location of the lava samples collected for this study. Their original locations and those of tephra are also reported in Supplementary Data 1. The relative ages of the lavas are based on ref. <sup>92</sup>.

cross stratified structures. We sampled juvenile lapilli fragments from the middle and upper parts of the section (c. 2.5 and 5 m from the base). More recently, late post-collapse pyroclastics (6) extend from 1.2 ka to historical times (e.g. Petroquines Tephra, El Soldado Eruptive Sequence, and Bueyes Tephra; PT, ESES, and BT, respectively; Fig. 2). Their bulk rock plus occasional glass groundmass geochemistry are also reported in the literature (i.e. ref. <sup>26</sup>).

**Geochemistry and texture of volcanic products.** The bulk rock composition of lavas and pyroclasts was determined using X-ray fluorescence (XRF) and compared with data from the literature (Supplementary Data 1 and Methods; e.g. refs. <sup>26,32</sup>). The chemistry of groundmass glass in pyroclasts and lavas was determined by electron probe microanalysis (EPMA; Supplementary Data 2 and Methods). For lava, it was only possible to measure residual glass between crystals with high-resolution chemical mapping (see Methods). There are clear compositional differences when comparing the pre- and post-collapse bulk rock compositions (Fig. 2a). The pre-collapse (Late Antuco) compositions are exclusively basalts and basaltic andesites, whereas the post-collapse products cover a broader range extending to more evolved compositions, with several high silica andesites and trachyandesites during the early post-collapse stage, and mainly basalts and basaltic andesites for the late post-collapse stage (Fig. 2a). Similarly, the pre- and late post-collapse glass compositions are of basaltic andesite composition, whereas a broad range of compositions from andesite, trachyandesite, and dacite are observed in the early post-collapse glasses of lavas and pyroclasts (Fig. 2b).

When plotted in a time series, the bulk rock compositions from the early post-collapse stage show increased SiO<sub>2</sub>, K<sub>2</sub>O, Na<sub>2</sub>O, and FeO, while CaO decreases compared to the previous and subsequent stages (Fig. 2c). Specifically, the bulk rock lavas during

the early post-collapse stage cover a larger compositional range, from 50.6 to 59.4 wt.% SiO<sub>2</sub>, relative to pre-collapse lavas. These changes suggest a period when silica-enriched melts were erupted, prior to returning to conditions like those that existed before the collapse. We observe a similar trend for pyroclasts, with tephra units  $\epsilon$  to EPT enriched in SiO<sub>2</sub>, K<sub>2</sub>O and Na<sub>2</sub>O compared to previous or subsequent pyroclastic units. However, there is a greater variability in the tephra compositions than in the lavas, with a reappearance of silica-rich compositions in samples the late post-collapse PT-top and -base units (Fig. 2c), and notably low bulk-rock silica (~50%; Fig. 2c) in the early post-collapse QDP unit. In the latter, the glass data spans from basaltic andesite to dacite, and we suspect these products may indicate a mixing of bimodal (mafic and silicic) magma compositions or the simultaneous interaction of different magmas within the same deposit.

The textural investigation of the Antuco lavas and pyroclasts reveals seriate textures with different crystal size populations including phenocrysts (>0.3 mm), microphenocrysts (0.03–0.3 mm) and microlites (<0.03 mm) (definitions after ref. <sup>33</sup>), which suggest magmas underwent crystallisation at different pressure and temperature conditions and/or involved multiple mixing episodes before eruption<sup>34</sup>. However, the early post-collapse PDC samples do not present disequilibrium textures. The vesicle-free phenocryst contents vary from 18 to 38% in these PDC pyroclasts and the most frequent mineral phases (in order of abundance) are plagioclase, olivine, and pyroxene, with minor iron-titanium oxides. The early post-collapse lavas never exceed 31% phenocrysts.

**Crystal textures and mineral chemistry.** At a microscale, the Antuco samples contain a variety of plagioclase phenocrysts, encompassing coarsely spongy cellular (sieve) texture either in the rim (type A) or the core (type B), but also crystals with step or patchy zoning (type C) and others that are homogeneous

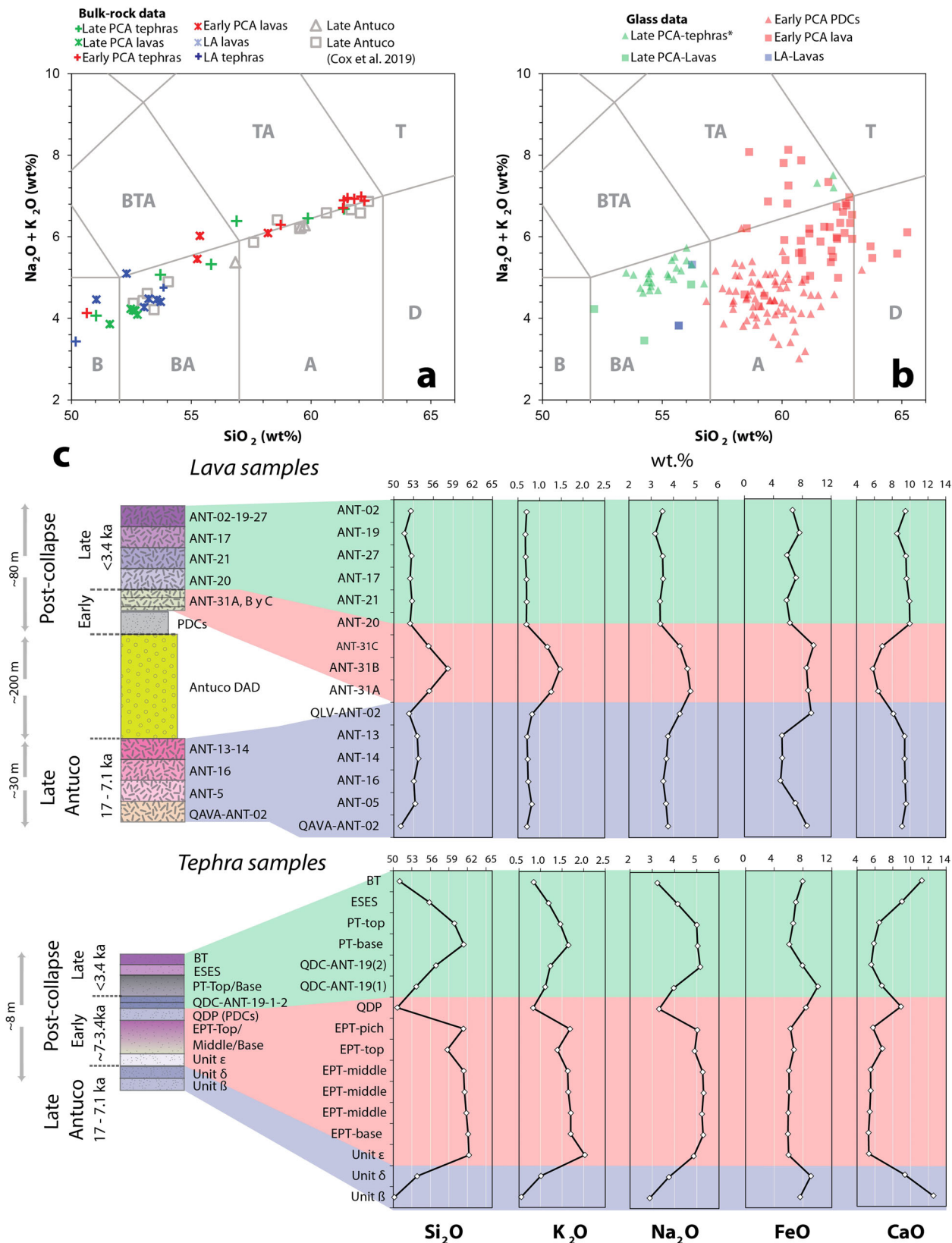


**Fig. 2** Compositional data of Antuco samples. Total alkali versus silica plot for bulk rock (a) and glass (b) showing compositions varying from basalt to dacite and trachyandesite. Letters represent basalt (B), basaltic andesite (BA), basaltic trachyandesite (BTA), andesite (A), trachyandesite (TA), trachyte (T) and dacite (D). **c** Time series of major oxide variations for bulk lava and pyroclast samples. Samples ANT-31B, C, and those from Late Antuco (LA) are from ref. 32.



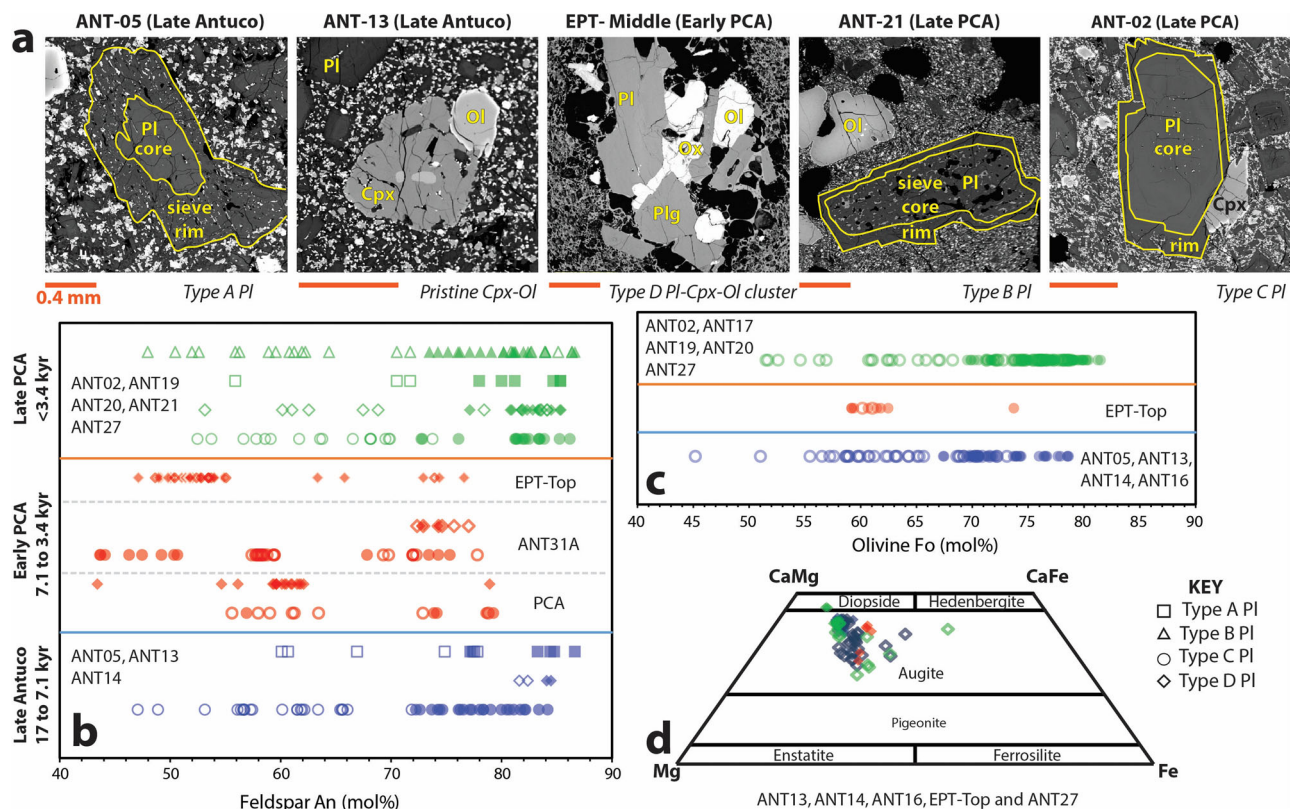


**Fig. 3** Crystal textures and their corresponding compositions in the Antuco products, from the pre-collapse (Late Antuco) to the early and late post-collapse stages. Filled symbols correspond to core compositions and open ones to rims. Different symbols are related to crystal types according to our textural classifications. **a** Types of crystal textures observed; plg, cpx, and ol refers to plagioclase, clinopyroxene, and olivine. **b** Feldspar anorthite composition for different crystal types during the evolution of Antuco volcano. **c** Olivine forsterite compositions for zoned crystals. **d** Pyroxene compositions for unzoned clinopyroxene crystals. The colour key is the same as in Fig. 2.

(Fig. 3a). The pre-collapse lavas (Late Antuco) show holocrystalline textures (no groundmass glass present), in which crystals have heterogeneous sizes. The early post-collapse products have porphyritic textures that contain scarce (<2 vol.%) plagioclase phenocrysts (up to 1.5 mm), which have tabular shapes and homogeneous composition. Abundant acicular swallow-tailed plagioclase and pyroxene crystals, with sizes <70  $\mu\text{m}$ , are observed in the groundmass. Pyroxene and olivine phenocrysts are euhedral and subhedral. Pyroxenes are homogeneous from a compositional point of view, whereas olivine exhibits normal progressive zoning. The late post-collapse products show porphyritic textures. Plagioclase and olivine phenocrysts (sizes up to 2.0 mm) have euhedral shapes. Coarse-sieve dominated plagioclase cores, partially resorbed, are exclusively observed in the late post-collapse stage. External rims around resorbed plagioclase cores indicate an overgrowth recorded by phenocrysts. We observe a groundmass that is either holocrystalline or partially glassy with swallow-tailed plagioclase crystals (<50  $\mu\text{m}$ ) and dendritic pyroxene crystals (<10  $\mu\text{m}$ ).

Compositionally, the plagioclase crystals of the pre-collapse and late post-collapse stages have cores with 72–87 mol. % anorthite (An), whereas the rims are An<sub>46–78</sub>, irrespective of the crystal texture (Fig. 3b; Supplementary Data 3). However, the early post-collapse plagioclases from the lavas and pyroclasts show the opposite trend with An-depleted cores and rims substantially An-enriched (Fig. 3b; Supplementary Data 3). Another important observation is that the maximum An content never exceeds 80 mol. % in these samples, in contrast to pre-collapse and late post-collapse anorthites that may reach up to 84 mol. %. Similar features are seen in the olivine compositions

(Fig. 3c) from pre- and late post-collapse stages: phenocryst cores have forsterite (Fo) contents of 67–84 mol. % and the rims reach Fo<sub><68</sub>, in contrast to the early post-collapse rims with Fo<sub><59</sub>. Unzoned clinopyroxene compositions are almost identical in the pre-, early post-collapse, and late post-collapse with CaMg-enriched augite in the cores to augite in the rims (Fig. 3d).

**History of magma storage.** We estimate the pre-eruptive magmatic dissolved water contents (Supplementary Data 4) by applying the plagioclase-liquid hygrometer (ref. 35) to our samples, informed by the most likely conditions governing the shallower magma system of Antuco in ref. 25. Water content estimates range from 2.5 to 3.2 wt. % for the pre-collapse products, from 1.4 to 5.1 wt. % for the early post-collapse products, and from 0.11 to 2.3 wt. % for the most recent eruptions (late post-collapse). For the whole data series, the median and average reach ~2.5 wt.% H<sub>2</sub>O, thus we consider that value as representative of the long-term system hydration at shallow conditions. To estimate the intensive magmatic conditions of these products, we used crystal-melt pairs in thermodynamic equilibrium (see Methods). Applying the feldspar-liquid (Supplementary Data 5) and the clinopyroxene-liquid geothermometers and geobarometers of ref. 36,37 (Supplementary Data 6) and the geothermometers of olivine-liquid and olivine-augite from refs. 36,38 (Supplementary Data 7) we obtained the crystallisation P-T conditions for cores and rims in these minerals (Fig. 4).

Irrespective of the crystal texture (either oscillatory zoned or sieve) and measurement position (crystal core or rim), the plagioclases from the pre-collapse stage indicate a narrow range of temperatures,

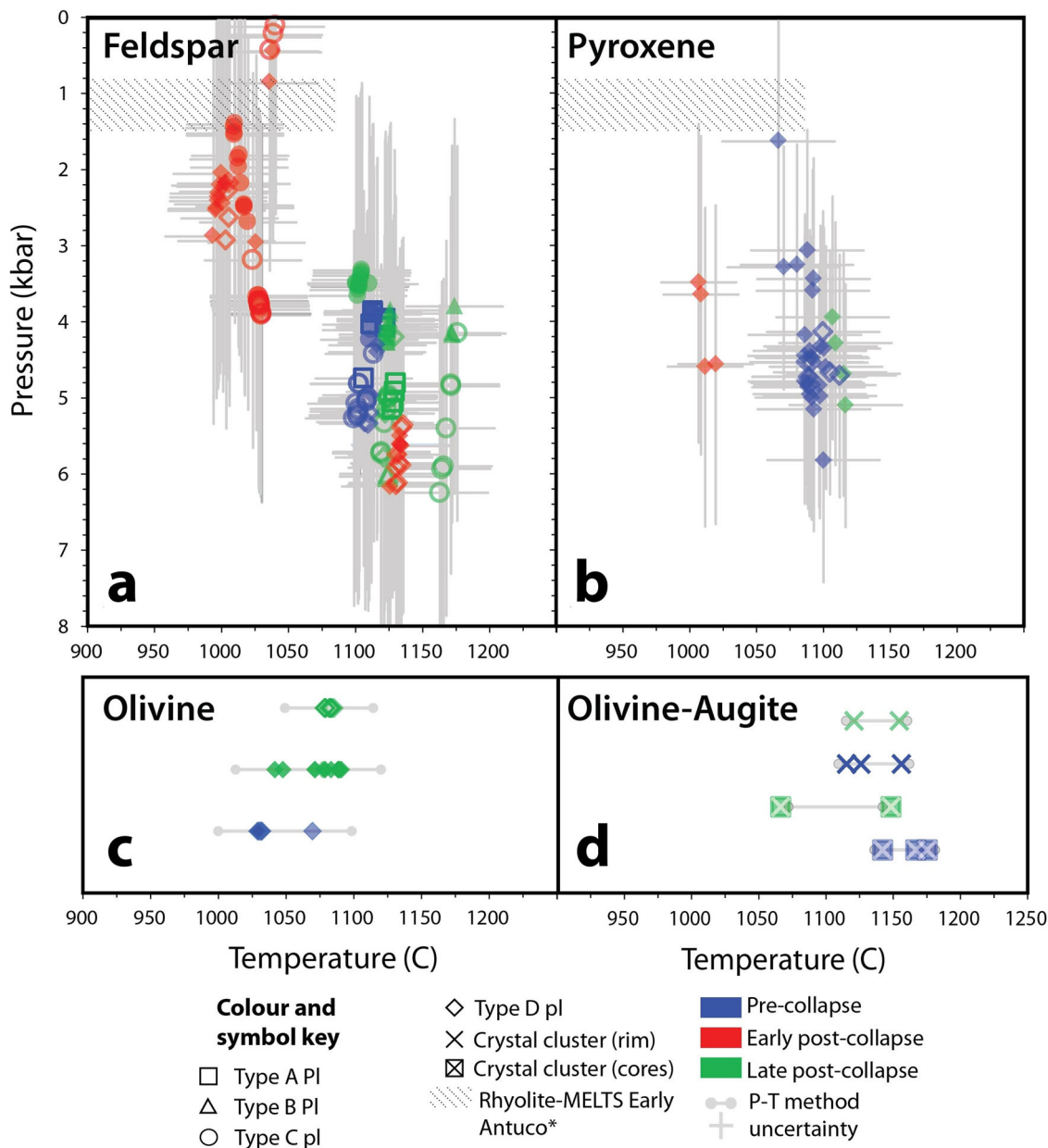


**Fig. 4** Pre-eruptive conditions for Antuco samples. **a** Feldspar-liquid geothermobarometers from ref. <sup>36,37</sup>. **b** Pyroxene geothermobarometers from ref. <sup>36,37</sup>. The grey error bars corresponds to the uncertainty of the equations. Filled symbols are crystal core data, whereas open ones represent rims. **c** Olivine-melt thermometry using the method of ref. <sup>36</sup> for pre- and late-post collapse samples. **d** Olivine-Augite thermometer of ref. <sup>38</sup>.

from 1098 to 1115 °C (Fig. 4a). Similarly, olivine-liquid and pyroxene-liquid pairs indicate temperatures in the range 1070–1112 °C and 1029–1070 °C, respectively (Fig. 4b, c). Contrastingly, estimates using olivine-augite thermometers return a range from 1115 to 1167 °C (Fig. 4d). The cores and rims of zoned plagioclase crystals of the early post-collapse samples (including lavas and pyroclasts) display the lowest temperatures, ranging from 1009 to 1040 °C, while in the unzoned plagioclase and pyroxene crystals, temperature estimates vary from ~1000 to 1020 °C (Fig. 4a, b). Finally, higher temperatures are again observed in the late post-collapse sieve plagioclase rims (1124–1128 °C), but especially on plagioclase cores and zoned plagioclase rims (1128–1183 °C).

The pressures obtained range from 3.2 to 6.2 kbar in the pre- and late post-collapse samples for all mineral phases. Conversely, the early post-collapse samples yield two other pressure ranges at 1.4–3.9 kbar and <0.8 kbar (Fig. 4a). Using the crustal density model for the southern Andes of ref. <sup>39</sup>, these *P* values are roughly

equivalent to storage depths for the pre-collapse and late-post collapse stages at 12–23 km, whereas the early post-collapse depths are 0–3.0 km and 5.3–14 km (Fig. 4a, b).

### Discussion and conclusion

A change in the composition of distinct volcanic products post-dating large-scale lateral collapses (>1.0 km<sup>3</sup>) has been previously documented in several other mafic volcanoes. For example, the compositionally narrow basaltic-andesitic magmas of Ritter Island (Papua New Guinea) were followed by a variety of basalts-to-rhyolites soon after its 1888 tsunamigenic collapse (ref. <sup>40</sup>; volume of 4.0–4.2 km<sup>3</sup>). In St. Lucia and Pitons du Carbet (Martinique, collapse <20 km<sup>3</sup>) post flank-collapse magmas are also more differentiated and crystalline than the pre-collapse ones<sup>41</sup>. Similarly, andesitic lavas of San Pedro volcano (southern Andes) were substituted by voluminous dacitic lavas containing basaltic inclusions

after a 4.0 km<sup>3</sup> collapse<sup>42</sup>. A corresponding pattern is observed at collapsed oceanic islands such as Fogo volcano (Cape Verde), with a 10 ka-long eruptive period of highly differentiated residual magmas after a huge lateral collapse (130–160 km<sup>3</sup>), followed by the restoration of conditions comparable to the pre-collapse stage since 60 ka<sup>27</sup>. Unlike these examples, small-scale lateral collapses (0.2–1.0 km<sup>3</sup>) are not usually followed by such compositional changes<sup>7,11</sup> and some do not change their eruptive styles at all after collapse<sup>20</sup>. In this respect, the Antuco collapse (6.4 km<sup>3</sup>) offers a good case study from which detailed evidence of the eruption of compositionally distinct volcanic products postdating its lateral collapse were collected. Our stratigraphically controlled sampling and the combination of different analytical techniques offers a unique chance of reconstructing long-term volcano development after edifice collapse.

To understand the driving forces behind the compositional change of Antuco, as a potential analogue for other arc stratovolcanoes affected by large-scale lateral collapses, it is necessary to consider the impact of collapse on magma storage conditions.

The normal zoning of olivine crystals, as well as step-normal zoning of plagioclase observed in the pre-collapse and late post-collapse stages, are indicative of crystallising melts that followed a liquid line of descent during cooling<sup>43,44</sup>. Sieve textures in plagioclase crystals are ubiquitous within the volcanic products of the late post-collapse stage, whereas they are present only at the rims of plagioclase crystals within the pre-collapse samples. Sieve textures are usually interpreted as produced either by magma decompression during ascent or magma mixing processes<sup>45</sup>. In this regard, the disequilibrium textures probably result from episodic rapid crystal dissolution induced by decompression during mafic magma ascent (generally ~52 wt.% SiO<sub>2</sub>) within the deep magma system (storage depths of 12–23 km), and elevated temperatures (1124–1183 °C). Hence, we suggest that the primary processes driving magma evolution in the system is cooling-driven crystallisation within a convective reservoir, interrupted by ascent-decompression events triggering crystal resorption-dissolution textures. These textures are absent within the early post-collapse plagioclase crystals, however the observed patchy zoning textures have been reproduced in cooling experiments<sup>44</sup> by small amounts of undercooling (e.g. 40 °C; using An<sub>60</sub> feldspar), and modest cooling rates (i.e.  $5.55 \times 10^{-4}$  °C s<sup>-1</sup>; with An<sub>40</sub> feldspar). Reverse zoning patterns shown by early post-collapse plagioclase crystals may represent decompression crystallisation or convection within a reservoir at temperatures from 950 to 1020 °C<sup>46</sup>, which agrees with our estimated temperatures. Moreover, the pressures we obtain show that these silicic magmas preserved in lavas (up to 59 wt.% SiO<sub>2</sub>) and pyroclasts (up to 62 wt.% SiO<sub>2</sub>) may have evolved in a shallow reservoir at <3.0 km. The more silicic nature of this reservoir is also supported by the plagioclase and olivine crystal compositions, which display lower anorthite and forsterite than for the pre- or late post-collapse stages. In this respect, the early post-collapse products indicate the stagnation, evolution, and late-stage decompression (either by ascent or by the unloading produced by the collapse) of relatively ‘cold’ magmas at shallow conditions, compared to those magmas erupted in the pre-collapse and late post-collapse stages.

To offer more insights into the effect of decompression of Antuco’s magma, we utilise two complementary theoretical and numerical approaches.

The loss of the cone material during collapse reduced the overburden pressure on the magma system, as expressed in the following form:

$$\sigma_{ov} = \int_0^z \rho \times g \times dz \quad (1)$$

Here,  $\rho$  is the density of the cone, assumed to be between 2000 and 2700 kg m<sup>-3</sup> (the latter is the highest for a compact vesicular

basalt; Schön, 2015),  $g$  is gravity acceleration and  $z$  is the minimum loss of material thickness, which in this case is 0.9 km at the volcano summit, according to ref. <sup>23</sup>. We therefore obtain decompression magnitudes between 0.18 and 0.24 kbar. Comparatively, the 1980 collapse of Mt. Saint Helens eliminated 0.6 km of the volcano summit and displaced nearly 2.5 km<sup>3</sup> of its flank, unloading the system by 0.25–0.3 kbar<sup>47,48</sup>. From experimental data, these unloading magnitudes are enough to trigger water exsolution and increase the plagioclase liquidus temperature in basalts, thus imposing an effective undercooling, crystallisation, and rising melt viscosity<sup>49</sup>. The enhanced crystallisation of mafic magmas not only changes the bulk rheology but also affects degassing efficiency, enhancing explosivity<sup>50</sup>.

Using the bulk rock compositions of our samples in addition to the temperatures obtained with the plagioclase-liquid thermometer, because these record the broadest range of temperatures in the dataset (Fig. 4a), we calculated the melt viscosity of the magma with the model of ref. <sup>51</sup>. We calculated that the melt viscosity increased from 10<sup>1</sup> to 10<sup>3</sup> (Pa s) during the early post-collapse stage in comparison to older and younger samples (10<sup>1</sup>–10<sup>2</sup> Pa s). Moreover, the bulk magma viscosity (considering crystal content) increased from 10<sup>4</sup> to 10<sup>6</sup> in the early post-collapse stage, according to the model of ref. <sup>52</sup> (Fig. 5). Hence, there is an empirical argument to support a rise in the magma viscosity after the lateral collapse. Conversely, the density calculated as in ref. <sup>53</sup> is lower for the early post-collapse magmas, which would have favoured ascent via system decompression.

The evolution of Antuco volcano offers another line of evidence in support of an unloading driven control on erupted magma compositions. The data of ref. <sup>25</sup> shows that andesitic lavas erupted at Antuco between 66 and 52 ka, and also during later stages of the pre-collapse edifice at 29.5 ± 7.5 and 15.5 ± 5.5 ka (Supplementary Discussion 1). The decreasing frequency of andesitic eruptions (i.e. relatively differentiated magma) through time was accompanied by an increase in the volume of the volcanic edifice from ~45 km<sup>3</sup> to 55 km<sup>3</sup>, during a period where glaciation would also have added to surface loading. Before the collapse, the Late Antuco stage built another 3–6 km<sup>3</sup> of exclusively basaltic products. This final volume is comparable to that removed by the avalanche (6.4 km<sup>3</sup>, ref. <sup>23</sup>), and the collapse-driven unloading is therefore compatible with the re-establishment of conditions that previously allowed more differentiated magma to erupt.

There is a possibility that the collapse ‘reactivated’ a shallower reservoir that already existed before the collapse. As shown in Fig. 4a, the source of the less differentiated pre-collapse and late post-collapse magmas corresponded to a hot and deep mafic reservoir, compared to the more differentiated (andesitic) early post-collapse magma sourced from a colder (~1000 °C) and shallower region at <3 km depth.

To investigate the influence of the collapse on the magma ascent dynamics, we used a 1D steady-state model of magma ascent in a cylindrical conduit<sup>54,55</sup>. The equations of the model controlling the fluid dynamics of magma ascent within the conduit have been illustrated by ref. <sup>56</sup>. To describe the magma ascent dynamics at Antuco volcano, appropriate constitutive equations (describing the specific rheological, solubility, outgassing, and fragmentation behaviour, together with equations of state for each component) have been also taken into account. Since our model is 1D, we cannot simulate exactly the magma ascent dynamics in complex plumbing systems. However, this is well-suited to describe the magma ascent dynamics of the shallower part of the plumbing system, where it is reasonable to assume a vertical cylindrical conduit. Furthermore, our model is steady-state, therefore it cannot reproduce the evolution of the eruption within short timescales (i.e. in the order of minutes). However, it



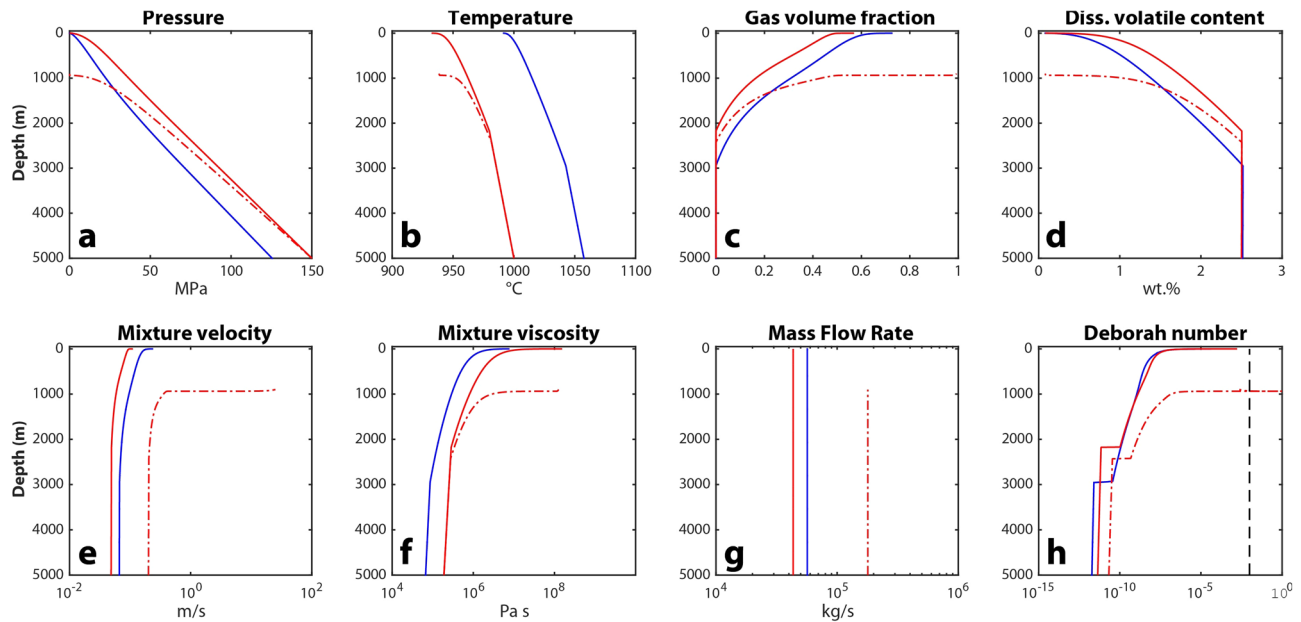


**Fig. 5 Conduit dynamics of Antuco volcano.** Evolution of (a) pressure, (b) temperature, (c) exsolved gas volume fraction, (d) dissolved volatile content, (e) mixture velocity, (f) mixture viscosity, (g) mass eruption rate (MER), and (h) Deborah number. The numerical results are retrieved from the conduit model for the pre- (blue line) and early post-collapse (red lines) situations of Antuco volcano, considering the pre-collapse composition is basaltic and the early post-collapse is andesitic. Only the upper 5 km of the conduit are shown for the basalt simulation which ascends from 15 km (Supplementary Fig. 2). The red dashed line corresponds to the unloaded edifice with a conduit 900 m shorter. That scenario is the only one able to produce an explosive eruption for the given conditions and shows a comparatively higher mass flow rate.

can be used to describe the magma ascent dynamics of long-lasting eruptions, where the dynamics occurring within the conduit have a much shorter timescale than the timescale of the eruption. Notwithstanding its limitations, it accurately describes most of the processes occurring during magma ascent towards surface, producing a realistic description of the magma ascent dynamics during volcanic eruptions. Indeed, this model, and its previous developments, have been used in the past to describe the magma ascent dynamics at several volcanic systems (such as Etna, Stromboli, Kilauea, Sunset Crater; refs. 55–59) [La Spina et al., 2016, 2017, 2019, 2021, 2022], so it is a perfect tool to investigate magma ascent dynamics at Antuco Volcano.

A more detailed description of the constitutive equations is reported in the Methods section. The initial conditions representative of the pre- and post-collapse stage of Antuco eruption have been inferred from the petrological data obtained within this work.

For the pre-collapse stage we simulated a deep (4 kbar) and hot magma reservoir (1130 °C) of basaltic composition (50.6 wt.% SiO<sub>2</sub>) with 38 vol.% crystal content and 15 km conduit length (Supplementary Data 8). The early post-collapse stage was simulated using an andesite magma (59.4 wt.% SiO<sub>2</sub>) stored at 1.5 kbar (i.e. at 5 km depth; ref. 25) with a temperature of 1000 °C and a 31 vol.% crystal content, but with a conduit length of only 4.1 km due to the collapse. Finally, to simulate the recovery of the volcanic edifice with time, the conduit length was restored to 5 km, i.e. the corresponding depth of an andesitic magma at 1.5 kbar (Supplementary Data 8). The H<sub>2</sub>O content for both stages was set to 2.5 wt.%, which is representative of the long-term system hydration at shallow conditions, as we suggested previously. For the different scenarios proposed, we ran the model considering conduits with radius of 5 and 10 m (as observed in the field from dykes intruding the pre-collapse edifice; ref. 60). The solutions with conduit of 10 m radius are shown in Fig. 5 (for a better comparison we plotted only the shallower 5 km of the conduit, even for the pre-collapse stage ascending

from 15 km depth), while those obtained assuming 5 m diameter are illustrated in Supplementary Fig. 1.

In Fig. 5a, b we illustrate the evolution of the pressure and temperature as magma ascends towards the surface. Due to the low H<sub>2</sub>O content (i.e. 2.5 wt.%), magma is undersaturated at depth, and volatile exsolution and expansion start to occur at ~3 km depth for the basaltic magma and ~2 km depth for the andesite magma (Fig. 5c, d). The basaltic magma ascends from 15 km depth towards the surface at low rates (Supplementary Fig. 2: from 0.06 at depth to 0.2 m s<sup>-1</sup> at the vent of the conduit) in about 60 h (Fig. 5e blue solid line; 18 h if we consider the upper 5 km of the conduit), increasing in viscosity from 10<sup>4</sup> to 10<sup>6</sup> Pa s (Fig. 5f blue solid line) and erupting effusively at 5.6 × 10<sup>4</sup> kg s<sup>-1</sup>. For the andesitic magma stored at 5 km depth that underwent sudden unloading by the collapse (i.e. with a conduit length of 4.1 km), the ascent rate is much faster (Fig. 5e; from 0.2 to 25 m s<sup>-1</sup>) reaching the surface only in 5 h. In that case the magma viscosity is higher (Fig. 5f; 10<sup>5</sup>–10<sup>8</sup> Pa s) and the magma erupts explosively (magma fragmentation is triggered when the Deborah number within the conduit exceeds 0.01, see Methods section) at ~2 × 10<sup>5</sup> kg s<sup>-1</sup> (Fig. 5g, h). Contrastingly, once the volcanic edifice is restored (i.e. the length of the conduit is set to 5 km) the same shallow andesitic magma ascends slowly (Fig. 5e; 0.05–0.1 m s<sup>-1</sup>) at low mass flow rates (Fig. 5f; ~4 × 10<sup>4</sup> kg s<sup>-1</sup>), consistent with the pre-collapse eruption conditions of basaltic magma, and without triggering fragmentation (Fig. 5h). Lower ascent rates favour gas/melt decoupling, preventing the formation of high strain rates, and thus fragmentation<sup>61</sup>. Our results do not intend to demonstrate that andesitic magma erupted explosively shortly after the collapse, but simply demonstrate that fast ascent of andesite magma is enabled by sudden decompression, and that conditions favouring explosive fragmentation are also plausible under the post-collapse conditions at Antuco. The post-collapse PDC deposits at Antuco directly overlie the debris avalanche deposit, and no indication of a time gap has been found between the two events. It is thus possible that the Antuco lateral collapse



was very shortly followed by explosive eruption. In a comparable example, the earthquake-triggered November 1964 collapse of Shiveluch in Kamchatka was followed by the explosive eruption of over pressurised andesitic magma minutes to hours later<sup>62</sup>, and we infer that a similar scenario is possible at Antuco. On the other hand, even though in our simulations we are assuming a constant crystal content, having a shorter conduit length produces a faster magma decompression and undercooling. This would lead to more extensive and more rapid crystallisation (ref. <sup>63</sup>), increasing magma bulk viscosity, although enhanced volatile exsolution may still favour fragmentation<sup>61</sup>. For hydrous andesitic magmas with comparable viscosities to those of Antuco's early post-collapse magmas, the observed flow rates characterise sub-Plinian eruptions (e.g. ref. <sup>64,65</sup>) because of high strain rates<sup>58</sup>. This is consistent with some of the tephra deposits found east of Antuco for this period (e.g. EPT unit, ref. <sup>26</sup>). Therefore, we can conclude that the more evolved compositions and increased pyroclastic activity observed in the early post-collapse stage are plausibly explained to result from sudden decompression caused by the collapse. During the progression of the early post-collapse stage, the edifice was gradually reconstructed by the explosive activity, progressively decreasing the relative overpressure. This rebuilding, combined with the exhaustion of over pressurised magma in the reservoir, may have produced a transition from dominantly explosive to dominantly effusive behaviour during the late post-collapse stage, as seen in the stratigraphy from ref. <sup>26</sup>. However, the change to dominantly effusive activity occurred before 3.4 ka, by the end of the early post-collapse stage, with the eruption of at least two andesitic lava flows lying on-top the PDC sequence. We infer that these silicic lavas represent buoyant portions of the more degassed residual andesitic magma.

In summary, both the petrochemical insights and numerical modelling illustrate that the decompressing effect of the collapse can account for the mobilisation of residual melts stored at shallow conditions (c. 5 km depth; Fig. 6). As shown by the work of ref. <sup>25</sup>, such a shallow reservoir may have existed long before the collapse during the Early Antuco stage, allowing the eruption and shallow intrusion of silicic magmas. Despite all the preserved silicic magmas for the Early Antuco correspond to lavas, it is very likely that explosive deposits were vanished by glacial erosion and are no longer preserved. According to previous numerical modelling of ref. <sup>66</sup>, andesitic melts can be produced by differentiation of basaltic melts on ka-timescales in stock-shaped magma bodies. We suggest that stagnant basaltic magmas may have differentiated in the shallower crust (ca. 5 km depth) to produce an andesitic reservoir. The sudden decompression of the reservoir enabled the andesitic magmas to ascend to the surface and erupt explosively, a condition that is reached if a strong decompression gradient is imposed upon these stagnant magmas. We suggest that this process would also have depleted the system of these transient, shallow, evolved magmas in the most recent history of Antuco. According to ref. <sup>25</sup>, during the late post-collapse phase, dense mafic magmas have been erupted at  $0.65\text{--}0.94\text{ km}^3\text{ ka}^{-1}$ , which represents about twice the estimated pre-collapse fluxes<sup>25</sup>. This led to rapid cone regeneration via dominantly effusive activity in a few thousand years, and a return to conditions that closely resemble those of the pre-collapse volcano. It should be noted that the magma plumbing system beneath Antuco may be structurally complex and would have developed over hundreds of thousands of years, a timescale longer than the cycle of destruction and regrowth considered here<sup>25</sup>. After 10 years of seismic recording, earthquake locations reveal an active area mostly concentrated around 5 km depth beneath Antuco (depths between 3 and 8 km; Supplementary Discussion 2). These earthquakes may represent a complex structural network belonging to the magmatic feeding system, with clusters of

seismicity potentially representing the top of the shallow magmatic reservoir recognised in this work.

Petrological studies suggest that evolved reservoirs in the shallow crust (i.e. andesitic-to-dacitic, <10 km depth) can be a common feature of dominantly mafic stratovolcanoes in arc systems (e.g. refs. <sup>67–71</sup>) or may develop by fractional crystallisation after periods of prolonged dormancy and edifice loading<sup>72</sup> (i.e. over thousands of years). More importantly, volcanoes with edifices higher than 2 km above their base are generally mafic and usually experience eruptions fed by the overpressure of a deep reservoir despite developing these more ephemeral shallow silicic reservoirs<sup>73</sup>. The mobilisation of magmas from stagnant shallower reservoirs could entirely modify the eruptive activity over timescales of thousands of years. This study of Antuco is important for understanding the magmatic processes that can occur in volcanoes reaching a critical edifice mass, to better explain the evolution of those volcanoes that have recently collapsed, and to refine volcano hazard and risk mitigation implications at potentially unstable volcanoes. This helps explain the evolution of volcanoes such as Chimborazo and Tungurahua (Ecuador), Nevado de Colima (Mexico), Ritter Island (Papua New Guinea), or the Secche di Lazzaro eruption at Stromboli (Italy), among others, from which unexpectedly silica-rich products were erupted soon after their lateral collapses<sup>9,14</sup>. Contrarily, other volcanoes have erupted rejuvenated magmas through predominantly effusive activity after their collapse (e.g. ref. <sup>14,74</sup>), probably as being fed by deep-seated reservoirs through mostly open-vent conduit dynamics, lacking shallower silicic reservoirs. The change of magma ascent dynamics that occurred at Antuco is illustrative of the eruption style transition towards an overall more explosive behaviour that can occur after a lateral collapse on a mafic volcano. We conclude that such changes in eruptive behaviour may last for thousands of years, and that collapse exerts an important control on volcanic evolution and that it can renew or change a volcanic hazard profile long beyond the collapse itself.

## Methods

**Sample collection.** Field surveys were carried out on in the austral summers between 2015 and 2021, with the aim of mapping and collecting representative samples from lava units and tephra fall deposits. We obtained fifteen lava samples from nine different lava units; each sample is represented by three hand-sized non-weathered rock fragments for textural and petrochemical investigation. Another three samples from three different pyroclastic units were also collected following the same scheme. These complement the existent data in ref. <sup>26</sup> that includes nine pyroclastic units. In total, this study covers eighteen volcanic units. A similar approach of exhaustive sample collection on the pre- and post-collapse volcanic units has been carried out for comparable studies (e.g. ref. <sup>19</sup>).

**Bulk rock geochemistry.** From nine lava samples, bulk-rock compositions were obtained using ICP Thermo Jarrell-Ash ENVIRO II housed at ActLabs (Canada). Samples were prepared in a mix of lithium metaborate and tetraborate, within an induction hob. The melt was immediately poured in a 5% nitric acid and then mixed to dissolution for 30 min. Seven other samples were analysed by X-Ray Fluorescence at the Department of Extractive Metallurgy of the National Polytechnic School of Ecuador (DEMEX-EPN). These correspond to two fresh lava clasts within the avalanche (a glassy basalt and fresh porphyritic andesite), two lava flows (pre- and post-collapse lavas, below and above the avalanche, respectively) and two scoria samples from tephra fall deposits recognised east of Antuco. Samples were crushed in an agate mortar (1 g) and then mixed with lithium metaborate. A melted bead was produced by using a platinum melting pot in the Katanax fusion fluxer. The glass beads were analysed using a Bruker S8 Tiger XRF instrument and the Spectra Plus software, identifying major oxides ( $\text{SiO}_2$ ,  $\text{Al}_2\text{O}_3$ ,  $\text{TiO}_2$ ,  $\text{MgO}$ ,  $\text{CaO}$ ,  $\text{Na}_2\text{O}$ ,  $\text{K}_2\text{O}$ ,  $\text{P}_2\text{O}_5$  and total  $\text{Fe}_2\text{O}_3$ ) with loss on ignition (LOI) values never higher than 2.06% (Supplementary Data 1). Total  $\text{Fe}_2\text{O}_3$  was converted to  $\text{FeO}$  and  $\text{Fe}_2\text{O}_3$ . Geochemical data were normalised to water and LOI free basis and was incremented with data found in the literature<sup>26,32</sup>. Similar methodologies and their resulting datasets have been previously used to compare pre- and post-collapse eruptive products at collapsed volcanoes (e.g. refs. <sup>14,19,41</sup>).

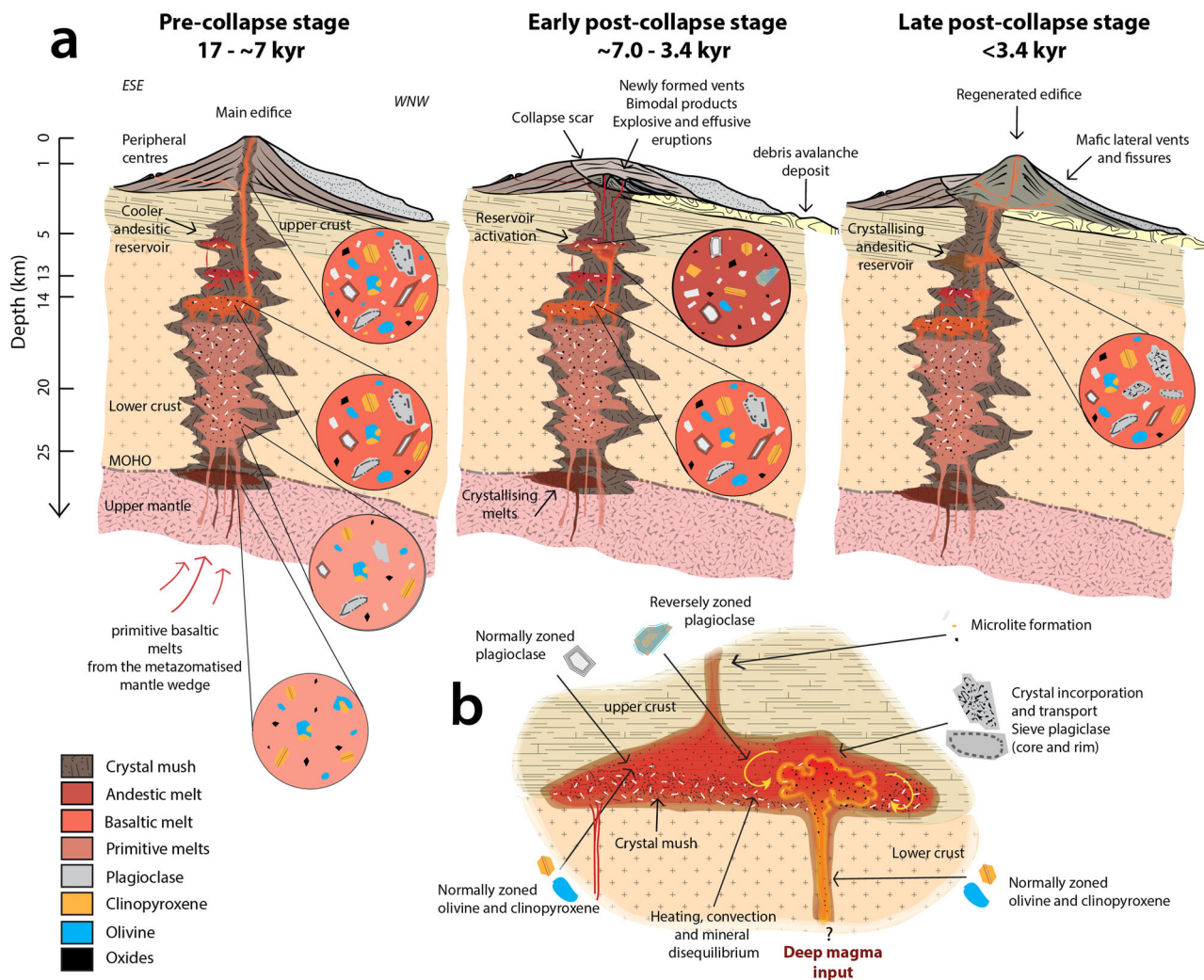


**Fig. 6** Cartoon illustrating the plumbing system of Antuco volcano. **a** Effect of the lateral collapse in decompressing silica-rich residual melts stored at a shallower region within the upper crust beneath the volcano. The different types of crystals and their configuration within the magma are represented in the circles. **b** These shallower reservoirs experienced cooling-crystallisation events and convection, that may ultimately have been driven by the input of small magma batches, to produce the variety of crystal textures observed in Antuco.

**Glass and crystal geochemistry.** Representative samples of scoria and lava were prepared as polished thin sections and/or polished sections mounted in epoxy resin, to be analysed using the FEI Quanta 650 FEG scanning electron microscope with energy dispersive X-Ray spectroscopy (SEM-EDS) at the Department of Earth and Environmental Sciences, University of Manchester (acceleration voltage of 15 kv and beam current to 10 nA).

To investigate crystal phases, and glassy groundmass major element compositions, we used two electron microprobes (EMPA), which allow collecting accurate quantitative data from igneous rocks, and have been used extensively to investigate the products of volcanic eruptions and the evolution of magmatic systems (e.g. refs. 11,20,26,42,46,65,67,68,70,71,73). We used the JXA-8530F FEG from the Photon Science Institute of the University of Manchester, and the JEOL JXA-8230 at Victoria University of Wellington. Both instruments were standardised with the same reference materials and operated under the same analytical conditions. For microlites and phenocrysts we used plagioclase NMNH115900, Kakanui augite USNM 122142, and synthetic oxides. Accelerating voltage was 15 kV, current of 12 nA, peak/background count times of 30/15 s, and a focused beam to 1  $\mu$ m. Major oxides for groundmass glasses were standardised against basaltic glass standard VGA-99 or NMNH 113716-1 for Ca, Mg, Fe; rhyolitic glass standard VG-568 for Si, Al, Na, K; synthetic oxides for Ti, Mn, Cr. Operating conditions for these were 15 kV, 8.0 nA, peak/background count times of 30/15 s, and a beam defocused to 10  $\mu$ m. For samples with higher amounts of microlites (e.g. EPT-Top, QDP and ANT31), the beam current was decreased to 5 nA and the diameter to 5 microns for the glass measurements; however, occasionally abundant microlites made it difficult to measure glass, thus we produced quant maps (100  $\times$  100px, 0.2microns/px, 200 ms dwell, ~2.5 h per area) to select specific pixels to be measured in the post-processing stage. To minimise sodium volatilisation during analysis of glasses, Na is measured first, and at a reduced peak/background count times of 10/5 s.

**Chemical and textural investigation.** During the post processing stage microprobe data were visualised along with the images captured via JEOL PC-SEM using Probelab ReImager<sup>75</sup>, which allows the location of point and shoot, PointID, and spectral mapping. The textural investigation of BSE images acquired at the SEM was carried out using the freeware JMicrovision<sup>76</sup>, which allows labelling the proportions of phenocrysts, glass, and vesicles through image processing techniques via the “Background Extraction” of pseudo-coloured BSE images.

**Geothermobarometry.** We used pairs of mineral phases and liquid in equilibrium as a proxy to estimate the pre-eruptive storage conditions: 148 plagioclase-liquid (Pl-liq), 41 olivine-liquid (Ol-liq), 39 clinopyroxene-liquid (Cpx-liq) and 20 olivine-augite (Ol-Aug) pairs. Crystal data retrieved from EPMA include both cores and rims and are classified depending on the type of crystal observed as well. Cations per formula unit (cfu) for all liquid components are calculated as anhydrous cation fractions<sup>36</sup>. Pl-liq, and Ol-liq equilibria are tested using  $K_D^{\text{An-Ab}}$  (Pl-liq) =  $0.27 \pm 0.18^{36}$  and  $K_D^{\text{Fe-Mg}}$  (Ol-liq) =  $0.3 \pm 0.03^{77}$ . Cpx-liq equilibrium is tested using the four criteria of ref. 37 with  $K_D^{\text{Fe-Mg}}$  (Cpx-liq) =  $0.28 \pm 0.03$ . The mineral-glass pairs are within 10% of Fe-Mg, DiHd component, CaTs component and Ti equilibrium according to equation 35 from ref. 38, the DiHd and CaTs equilibrium and the Ti partitioning model (ref. 37 and references therein; Supplementary Data 6). Clinopyroxene cfu is calculated on a 6-oxygen basis, those with total cfu outside the range  $4.0 \pm 0.02$  were discarded and the method of ref. 78 was used to calculate the ratio of Fe<sup>2+</sup> to Fe<sup>3+</sup>. Liquid composition used corresponds to glass or bulk rock composition depending on the suitability. In general, bulk rock was used for lavas whereas crystals in pyroclasts are in equilibrium with their corresponding glasses. For the feldspar-liquid method, the standard error of estimate (SEE) for T and P are 36 °C and 2.8 kbar, respectively, whereas the

clinopyroxene liquid has SEEs of 42 °C and 1.6 kbar, respectively<sup>36,37</sup>. According to ref. 79, the Cpx-liq eq33 from ref. 36 used in this work performs well for arc magmas and informs good constraints of the magma storage temperature, however the barometer used (ref. 37) is only affordable to distinguish whether a Cpx formed in the upper crust or not. The olivine-liquid and olivine-augite thermometers display T SEEs of 29 °C and 6 °C, respectively<sup>36,38</sup>.

**Constitutive equations for the magma ascent model.** To simulate the conduit dynamics experienced by Antuco's magmas during the pre- and post-collapse eruptive scenarios, we adopted the 1-D steady state conduit model illustrated in ref. 56. This model is able to calculate all of the major processes occurring during magma ascent, such as the temperature changes, viscosity evolution, non-ideal gas exsolution and expansion, outgassing, and magma fragmentation for an ascending magma at different depths<sup>56</sup>. This model has been used in previous works to characterise magma ascent dynamics at different volcanoes (e.g. refs. 54–56,59). The governing equations of the model, i.e. the equations that control the fluid dynamics of the magmatic mixture, have been reported in ref. 56. To describe the magma ascent dynamics at Antuco volcano we adopted a series of specific constitutive equations that well represent the rheology, solubility, wall-friction forces, outgassing, and fragmentation for this volcanic system.

The viscosity of the liquid mixture ( $\mu_l$ ) is calculated as the viscosity of the crystal-free liquid phase ( $\mu_{melt}$ ) multiplied by a factor ( $\theta_c$ ) considering the increase in viscosity due to the presence of crystals<sup>80</sup>. Following the model of ref. 51 we estimate  $\mu_{melt}$  as a function of melt composition, water concentration and temperature. To better describe the viscosity of the crystal-free melt during the pre- and post-collapse phases at Antuco we used the compositions reported in Supplementary Data 8. The factor  $\theta_c$ , instead, considers the presence of crystals as described in ref. 81.

$$\theta_c = \frac{1 + \varphi^\delta}{[1 - F(\varphi, \xi, \gamma)]^{B\varphi^*}},$$

where

$$F = (1 - \xi) \operatorname{erf} \left[ \frac{\sqrt{\pi}}{2(1 - \xi)} \varphi(1 + \varphi^\gamma) \right]; \varphi = \frac{\phi_{tot}}{\phi^*}.$$

In previous equations  $\phi_{tot}$  is the total crystal content in the magma (assumed to be constant for this work), and  $B, \delta, \xi, \gamma$  and  $\phi^*$  are empirical parameters. Here we used the same empirical parameters ( $B, \delta, \xi, \gamma$  and  $\phi^*$ ) as in ref. 53; i.e.  $B = 2.8$ ,  $\delta = 13 - \gamma$ ,  $\xi = 0.0327$ ,  $\gamma = 0.84$  and  $\phi^* = 0.274$ . The total crystal content assumed for the pre- and post-collapse stages of Antuco is 0.38 and 0.30, respectively, in agreement with the maximum crystal fractions observed in natural samples from these stages.

Since there are no information on the amount of CO<sub>2</sub> present in the Antuco volcanic system, for this work we considered a single gas component, i.e. only water. The amount of water dissolved within the melt ( $x_d$ ) has been calculated as an exponential function of the magma pressure:

$$x_d = \sigma P^\epsilon$$

where  $\sigma$  and  $\epsilon$  are the solubility coefficient and solubility exponent, respectively. In agreement with ref. 64 we set  $\sigma = 1.8911 \times 10^{-6}$ , and  $\epsilon = 0.5257$ .

According to magma ascent rate and Reynolds number of ascent (Re), laminar or turbulent flow regimes may develop. For  $Re < 2000$  a laminar flow is assumed, and the liquid phase friction factor is computed using the Hagen-Poiseuille's law:

$$f_{D_i}^{laminar} = \frac{64}{Re}$$

For  $Re > 3000$ , instead, a turbulent flow regime is considered, and, following the equation of ref. 82, the friction factor is calculated as follows:

$$f_{D_i}^{turbulent} = 1.613 \left[ \ln \left( 0.23 Rr^{1.1007} - \frac{60.525}{Re^{1.1105}} + \frac{56.291}{Re^{1.0712}} \right) \right]^{-2}$$

where  $Rr$  is the relative roughness of the pipe and its value is 0.05 according to ref. 54. In the transitional regime, i.e. when  $Re$  is between 2000 and 3000, the friction factor is calculated as a linear interpolation between  $f_{D_i}^{laminar}$  and  $f_{D_i}^{turbulent}$ . Above the fragmentation level, gas-wall drag  $f_{D_g}$  is set to 0.03 as in ref. 83.

The efficiency of gas escape during magma ascent is a key control of explosivity<sup>84,85</sup>. In the magma ascent model adopted here we only consider the vertical gas loss, whereas lateral gas escape is not taken into account. In general, lateral degassing is thought to occur when conduit pressure is greater than lithostatic pressure and the gas volume fraction exceeds a critical value (usually assumed to be 0.6)<sup>86,87</sup>. For dome building eruptions, where the pressure within the conduit is significantly higher than lithostatic pressure, and magma ascent rate is very low ( $< 10^3 \text{ kg s}^{-1}$ ), lateral gas loss can be important (e.g. refs. 84,88,89). However, for the type of activity we are describing here, where mass eruption rate is in the order of  $10^5 \text{ kg s}^{-1}$  and conduit pressure is not significantly higher than lithostatic pressure, it is reasonable to assume, as a first order approximation, that lateral gas loss is negligible. By looking at the numerical results (Fig. 5c), we can also infer that, even considering lateral gas flow, it would have been taking place

just few meters below the vent, where the gas volume fraction exceeds the critical value of 0.6, and thus not affecting most of magma ascent from depth.

Below the fragmentation level, the relative motion between gas and melt is described using a permeable gas flow regime (in which gas flows through interconnected pathways within the melt), whereas above the fragmentation level we used the drag model for the gas-ash flow adopted by ref. 90.

For the permeable gas flow regime, we used the Forchheimer's law<sup>85</sup>, which is a function of viscous and inertial permeabilities. The viscous permeability ( $k_v$ ) is calculated as in ref. 90:

$$k_v = \frac{(f_{tb} r_b)^2}{8} \alpha_g^m$$

where  $f_{tb}$  is the throat-bubble size ratio,  $m$  is the tortuosity factor,  $r_b$  is the average bubble size, and  $\alpha_g$  is the gas volume fraction. The average bubble size  $r_b$  is calculated assuming a constant bubble number density ( $N_d$ ) as in ref. 85:

$$r_b = \left( \frac{\alpha_g}{\frac{4\pi}{3} N_d \alpha_1} \right)^{\frac{1}{3}}$$

The inertial permeability ( $k_i$ ) is calculated using the following equation of ref. 85:

$$k_i = \frac{f_{tb} r_b}{f_0} \alpha_g^{\frac{1+3m}{2}}$$

where  $f_0$  is a friction coefficient. Here we used the following values:  $f_{tb} = 0.8$ ,  $m = 5$ ,  $N_d = 10^{11}$  and  $f_0 = 10^{-5}$ .

Finally, magma fragmentation is the process that characterises the transition from ductile to brittle behaviour of magma. This is thought to occur when the timescale of deformation of magma ( $\lambda_d$ ) is much smaller than the Maxwell relaxation timescale ( $\lambda_r$ ). Specifically, by defining the Deborah number ( $De$ ) as the ratio between the Maxwell relaxation timescale  $\lambda_r$ , and the timescale of deformation  $\lambda_d$ , it has been seen experimentally that magma fragmentation occurs when  $De \geq 0.01$ <sup>91</sup>.

$$De = \frac{\lambda_r}{\lambda_d} = \frac{\left( \frac{\mu_l}{G_\infty} \right)}{\left( \frac{1}{\dot{\gamma}} \right)} = \frac{\mu_l \dot{\gamma}}{G_\infty} \geq 0.01$$

Here,  $\mu_l$  is the magma bulk viscosity,  $\dot{\gamma}$  is the strain rate and  $G_\infty$  is the unrelaxed shear modulus at infinite frequency of the magma<sup>90</sup>, which for a basaltic magma  $G_\infty = 10^{10} \text{ Pa}$  can be assumed.

## Data availability

The authors declare that all other relevant data supporting the findings of this study are included in the paper, in the Supplementary Data, Figures and in the Supplementary Discussion 1 and 2. All data used in this paper is found at <https://doi.org/10.6084/m9.figshare.c.6707292.v1>.

## Code availability

The magma ascent model used in this study has been adapted from the MAMMA model available on GitHub: <https://github.com/demichie/MAMMA>.

Received: 2 February 2023; Accepted: 13 July 2023;

Published online: 16 August 2023

## References

1. Finn, C., Sisson, T. & Deszcz-Pan, M. Aerogeophysical measurements of collapse-prone hydrothermally altered zones at Mount Rainier volcano. *Nature* **409**, 600–603 (2001).
2. van Wyk de Vries, B. & Francis, P. Catastrophic collapse at stratovolcanoes induced by gradual volcano spreading. *Nature* **387**, 387–390 (1997).
3. Giampiccolo, E. et al. Dyke intrusion and stress-induced collapse of volcano flanks: The example of the 2018 event at Mt. Etna (Sicily, Italy). *Sci. Rep.* **10**, 6373 (2020).
4. Pierson, T. C. & Costa, J. E. A rheologic classification of subaerial sediment-water flows. *Geol. Soc. Am. Rev. Eng. Geol.* **7**, 1–12 (1987).
5. Scott, K. M. et al. Catastrophic Debris flows transformed from landslides in volcanic terrains: mobility, hazard assessment, and mitigating strategies. *U.S. Geol. Survey Professional Paper* **1630**, 59 (2001).
6. Siebert, L., Glicken, H. & Ui, T. Volcanic hazards from Bezymianny-and Bandai-type eruptions. *Bullet. Volcanol.* **49**, 435–459 (1987).
7. Romero, J. E. et al. Volcanic Lateral Collapse Processes in Mafic Arc Edifices: A Review of Their Driving Processes, Types and Consequences. *Front. Earth Sci.* **9**, 639825 (2021).
8. Zernack, A. V., Procter, J. N. Cyclic Growth and Destruction of Volcanoes. In: (eds Roverato M., Dufresne A., Procter J.) *Volcanic Debris Avalanches*.



- Advances in Volcanology*. Springer, Cham. [https://doi.org/10.1007/978-3-030-57411-6\\_12](https://doi.org/10.1007/978-3-030-57411-6_12) (2021).
9. Bertagnini, A. & Landi, P. The Secche di Lazzaro pyroclastics of Stromboli volcano: a phreatomagmatic eruption related to the Sciara del Fuoco sector collapse. *Bull Volcanol.* **58**, 239–245 (1996).
  10. Belousov, A., Voight, B. & Belousova, M. Directed blasts and blast-generated pyroclastic density currents: a comparison of the Bezymianny 1956, Mount St Helens 1980, and Soufrière Hills, Montserrat 1997 eruptions and deposits. *Bull Volcanol.* **69**, 701–740 (2007).
  11. Cutler, K. S. et al. Downward-propagating eruption following vent unloading implies no direct magmatic trigger for the 2018 lateral collapse of Anak Krakatau. *Earth Planet Sci. Lett.* **578**, 117332 (2022).
  12. Pinel, V. & Jaupart, C. Some consequences of volcanic edifice destruction for eruption conditions. *J. Volcanol. Geotherm. Res.* **145**, 68–80 (2005).
  13. Pinel, V. & Albino, F. Consequences of volcano sector collapse on magmatic storage zones: insights from numerical modeling. *J. Volcanol. Geotherm. Res.* **252**, 29–37 (2013).
  14. Watt, S. F. The evolution of volcanic systems following sector collapse. *J. Volcanol. Geotherm. Res.* **384**, 280–303 (2019).
  15. Tibaldi, A. Major changes in volcano behaviour after a sector collapse: insights from Stromboli, Italy. *Terra Nova* **16**, 2–8 (2004).
  16. Manconi, A. et al. The effects of flank collapses on volcano plumbing systems. *Geology* **37**, 1099–1102 (2009).
  17. Maccaferri, F., Richter, N. & Walter, T. R. The effect of giant lateral collapses on magma pathways and the location of volcanism. *Nat. comm.* **8**, 1–11 (2017).
  18. Shevchenko, A. V. et al. The rebirth and evolution of Bezymianny volcano, Kamchatka after the 1956 sector collapse. *Commun. Earth Environ.* **1**, 15 (2020).
  19. Cornu, M. N. et al. Exploring the links between volcano flank collapse and the magmatic evolution of an ocean island volcano: Fogo, Cape Verde. *Sci. Rep.* **11**, 1–12 (2021).
  20. Romero, J. E. et al. The initial phase of the 2021 Cumbre Vieja ridge eruption (Canary Islands): Products and dynamics controlling edifice growth and collapse. *J. Volcanol. Geotherm. Res.* **431**, 107642 (2022b).
  21. Calder, E., Wagner, K., Ogburn, S. Volcanic hazard maps. In: (eds Loughlin S., Sparks S., Brown S., Jenkins S., Vye-Brown C.) Global volcanic hazards and risk. Cambridge University Press, 335–342 (2015).
  22. Procter, J. N., Zernack, A. V., Cronin, S. J. Computer Simulation of a Volcanic Debris Avalanche from Mt. Taranaki, New Zealand. In: (eds Roverato M., Dufresne A., Procter J.) Volcanic Debris Avalanches. *Advances in Volcanology*. Springer, Cham. [https://doi.org/10.1007/978-3-030-57411-6\\_11](https://doi.org/10.1007/978-3-030-57411-6_11) (2021).
  23. Romero, J. E., Moreno, H., Polacci, M., Burton, M., Guzmán, D. Mid-Holocene lateral collapse of Antuco volcano (Chile): debris avalanche deposit features, emplacement dynamics, and impacts. *Landslides* **19**, 1321–1338 (2022a).
  24. López-Escobar, L., Vergara, M. & Frey, F. A. Petrology and geochemistry of lavas from Antuco volcano, a basaltic volcano of the southern Andes (37° 25' S). *J. Volcanol. Geotherm. Res.* **11**, 329–352 (1981).
  25. Martínez, P., Singer, B. S., Moreno, H. & Jicha, B. R. Volcanologic and petrologic evolution of Antuco-Sierra Velluda, Southern Andes, Chile. *J. Volcanol. Geotherm. Res.* **349**, 392–408 (2018).
  26. Romero, J. E. et al. Pyroclastic deposits and eruptive heterogeneity of Volcán Antuco (37° S; Southern Andes) during the Mid to Late Holocene (<7.2 ka). *J. Volcanol. Geotherm. Res.* **392**, 106759 (2020).
  27. Longpré, M. A., Troll, V. R., Walter, T. R., Hansteen, T. H. Volcanic and geochemical evolution of the Teno massif, Tenerife, Canary Islands: Some repercussions of giant landslides on ocean island magmatism. *Geochem. Geophys. Geosystems.* **10**, 12017 (2009).
  28. Boulesteix, T., Hildenbrand, A., Gillot, P. Y. & Soler, V. Eruptive response of oceanic islands to giant landslides: new insights from the geomorphologic evolution of the Teide–Pico Viejo volcanic complex (Tenerife, Canary). *Geomorphology* **138**, 61–73 (2012).
  29. Gimbre, C. & Wörner, G. Variable parent magmas and recharge regimes of the Paríacota magma system (N. Chile) revealed by Fe, Mg and Sr zoning in plagioclase. *Lithos* **98**, 118–140 (2007).
  30. Blundy, J. et al. Evolving magma storage conditions beneath Mount St. Helens inferred from chemical variations in melt inclusions from the 1980–1986 and current (2004–2006) eruptions. *US Geol. Survey Professional Paper* **1750**, 755–790 (2008).
  31. Turner, S. J., Izbekov, P. & Langmuir, C. The magma plumbing system of Bezymianny Volcano: insights from a 54 year time series of trace element whole-rock geochemistry and amphibole compositions. *J. Volcanol. Geotherm. Res.* **263**, 108–121 (2013).
  32. Cox, D. et al. Chalcophile element processing beneath a continental arc stratovolcano. *Earth Planet Sci. Lett.* **522**, 1–11 (2019).
  33. Zellmer, G. F. Gaining acuity on crystal terminology in volcanic rocks. *Bull Volcanol.* **83**, 1–8 (2021).
  34. Gill, R. *Igneous rocks and processes: a practical guide*. (John Wiley & Sons, 2011).
  35. Waters, L. E. & Lange, R. A. An updated calibration of the plagioclase-liquid hygrometer-thermometer applicable to basalts through rhyolites. *Am. Min.* **100**, 2172–2184 (2015).
  36. Putirka, K. D. Thermometers and barometers for volcanic systems. *Rev. Mineral Geochem.* **69**, 61–120 (2008).
  37. Neave, D. A. & Putirka, K. D. A new clinopyroxene-liquid barometer, and implications for magma storage pressures under Icelandic rift zones. *Am. Miner.* **102**, 777–794 (2017).
  38. Loucks, R. R. A precise olivine-augite Mg-Fe-exchange geothermometer. *Contrib. Mineral Petrol.* **125**, 140–150 (1996).
  39. Tassara, A., Götz, H. J., Schmidt, S., Hackney, R. Three-dimensional density model of the Nazca plate and the Andean continental margin. *J. Geophys. Res.: Solid Earth*, **111**, B09404 (2006).
  40. Watt, S. F. et al. From catastrophic collapse to multi-phase deposition: flow transformation, seafloor interaction and triggered eruption following a volcanic-island landslide. *Earth Planet Sci. Lett.* **517**, 135–147 (2019).
  41. Boudon, G. et al. Role of large flank-collapse events on magma evolution of volcanoes. Insights from the Lesser Antilles Arc. *J. Volcanol. Geotherm. Res.* **263**, 224–237 (2013).
  42. Costa, F. & Singer, B. Evolution of Holocene dacite and compositionally zoned magma, Volcán San Pedro, southern volcanic zone, Chile. *J. Petrol.* **43**, 1571–1593 (2002).
  43. Lofgren, G. & Hargraves, R. B. Experimental studies on the dynamic crystallization of silicate melts. *Phys. Magm. Processes* **487**, 551 (1980).
  44. Streck, M. J. Mineral textures and zoning as evidence for open system processes. *Rev. Mineral Geochem.* **69**, 595–622 (2008).
  45. Nelson, S. T. & Montana, A. Sieve-textured plagioclase in volcanic rocks produced by rapid decompression. *Am. Mineralogist* **77**, 1242–1249 (1992).
  46. Ustunisik, G., Kilinc, A. & Nielsen, R. L. New insights into the processes controlling compositional zoning in plagioclase. *Lithos* **200**, 80–93 (2014).
  47. Glicken, H. *Rockslide-debris avalanche of May 18, 1980, Mount St. Helens volcano, Washington*. Doctoral dissertation, (University of California, Santa Barbara, 1986).
  48. Blundy, J. & Cashman, K. Rapid decompression-driven crystallization recorded by melt inclusions from Mount St. Helens volcano. *Geology* **33**, 793–796 (2005).
  49. Arzilli, F. et al. Plagioclase nucleation and growth kinetics in a hydrous basaltic melt by decompression experiments. *Contrib. Mineral Petrol.* **170**, 1–16 (2015).
  50. Lindoo, A., Larsen, J. F., Cashman, K. V. & Oppenheimer, J. Crystal controls on permeability development and degassing in basaltic andesite magma. *Geology* **45**, 831–834 (2017).
  51. Giordano, D., Russell, J. K. & Dingwell, D. B. Viscosity of magmatic liquids: a model. *Earth Planet Sci. Lett.* **271**, 123–134 (2008).
  52. Vona, A., Romano, C., Dingwell, D. B. & Giordano, D. The rheology of crystal-bearing basaltic magmas from Stromboli and Etna. *Geochim. et Cosmochim. Acta* **75**, 3214–3236 (2011).
  53. Iacovino, K., Till, C. B. DensityX: A program for calculating the densities of magmatic liquids up to 1627 °C and 30 kbar. *Volcanica* **2**, 1–10 (2019).
  54. La Spina, G., Burton, M. & Vitturi, M. D. M. Temperature evolution during magma ascent in basaltic effusive eruptions: A numerical application to Stromboli volcano. *Earth Planet Sci. Lett.* **426**, 89–100 (2015).
  55. La Spina, G. et al. Conduit dynamics of highly explosive basaltic eruptions: The 1085 CE Sunset Crater sub-Plinian events. *J. Volcanol. Geotherm. Res.* **387**, 106658 (2019).
  56. La Spina, G. et al. Role of volatiles in highly explosive basaltic eruptions. *Commun. Earth Environ.* **3**, 1–13 (2022).
  57. La Spina, G., Burton, M., de' Michieli Vitturi, M., Arzilli, F. Role of syn-eruptive plagioclase disequilibrium crystallization in basaltic magma ascent. *Nat. Commun.* **7**, 1–10 (2016).
  58. La Spina, G., Polacci, M., Burton, M., de' Michieli Vitturi, M. Numerical investigation of permeability models for low viscosity magmas: application to the 2007 Stromboli effusive eruption. *Earth Planet Sci. Lett.* **59** (2017)
  59. La Spina, G. et al. Explosivity of basaltic lava fountains is controlled by magma rheology, ascent rate and outgassing. *Earth Planetary Sci. Lett.* **553**, 116658 (2021).
  60. Belousov, A. B. The Shiveluch volcanic eruption of 12 November 1964—explosive eruption provoked by failure of the edifice. *J. Volcanol. Geotherm. Res.* **66**, 357–365 (1995).
  61. Pyle, D. M. Sizes of volcanic eruptions. In *The encyclopedia of volcanoes*. 257–264. (Academic Press, 2015).
  62. Lohmar, S. Estratigrafía, petrografía y geoquímica del volcán Antuco y sus depósitos (Andes del Sur, 37°25'S). Memoria de Título (Unpublished), (Universidad de Concepción, Departamento de Ciencias de la Tierra, Concepción, 2000).

63. Arzilli, F. et al. Magma fragmentation in highly explosive basaltic eruptions induced by rapid crystallization. *Nat. Geosci.* **12**, 1023–1028 (2019b).
64. Romero, J. E. et al. Eruption dynamics of the 22–23 April 2015 Calbuco Volcano (Southern Chile): Analyses of tephra fall deposits. *J. Volcanol. Geotherm. Res.* **317**, 15–29 (2016).
65. Arzilli, F. et al. The unexpected explosive sub-Plinian eruption of Calbuco volcano (22–23 April 2015; southern Chile): Triggering mechanism implications. *J. Volcanol. Geotherm. Res.* **378**, 35–50 (2019a).
66. Gutiérrez, F. & Parada, M. A. Numerical modeling of time-dependent fluid dynamics and differentiation of a shallow basaltic magma chamber. *J. Petrol.* **51**, 731–762 (2010).
67. Tormey, D. R., Frey, F. A. & López-Escobar, L. Geochemistry of the active Azufre—Planchon—Petroera volcanic complex, Chile (35°15′ S): evidence for multiple sources and processes in a cordilleran arc magmatic system. *J. Petrol.* **36**, 265–298 (1995).
68. Gilbert, D., Freundt, A., Kutterolf, S. & Burkert, C. Post-glacial time series of explosive eruptions and associated changes in the magma plumbing system of Lonquimay volcano, south central Chile. *Int. J. Earth Sci.* **103**, 2043–2062 (2014).
69. Kaneko, T., Yasuda, A., Fujii, T. & Yoshimoto, M. Crypto-magma chambers beneath Mt. Fuji. *J. Volcanol. Geotherm. Res.* **193**, 161–170 (2010).
70. Bechon, T. et al. Petrology of the magmatic system beneath Osorno volcano (Central Southern Volcanic Zone, Chile). *Lithos* **426**, 106777 (2022).
71. Boschetty, F. O. et al. Insights into magma storage beneath a frequently erupting arc volcano (Villarrica, Chile) from unsupervised machine learning analysis of mineral compositions. *Geochem. Geophys. Geosyst.* **23**, e2022GC010333 (2022).
72. Singer, B. S. et al. Lying in wait: deep and shallow evolution of dacite beneath Volcán de Santa María, Guatemala. *Geol. Soc. Spec. Publ.* **385**, 209–234 (2014).
73. Castruccio, A., Diez, M. & Gho, R. The influence of plumbing system structure on volcano dimensions and topography. *J. Geophys. Res.: Solid Earth* **122**, 8839–8859 (2017).
74. Hora, J. M., Singer, B. S. & Wörner, G. Volcano evolution and eruptive flux on the thick crust of the Andean Central Volcanic Zone: 40Ar/39Ar constraints from Volcán Parímacota, Chile. *Geol. Soc. Am. Bull.* **119**, 343–362 (2007).
75. Kraft, N. & von der Handt, A. Probelab Relmager: An Open-Source Software for Streamlining Image Processing in an Electron Microscopy Laboratory. *Microscopy Today* **29**, 38–41 (2021).
76. Roduit, N. JMicroVision: Image analysis toolbox for measuring and quantifying components of high-definition images. *Ver.* **1**, 2002–2007 (2008).
77. Roeder, P. L. & Emslie, R. F. Olivine-liquid equilibrium. *Contrib. Mineral Petrol* **29**, 275–289 (1970).
78. Droop, G. T. R. A general equation for estimating Fe<sup>3+</sup> concentrations in ferromagnesian silicates and oxides from microprobe analyses, using stoichiometric criteria. *Mineral Mag.* **51**, 431–435 (1987).
79. Wieser, P., Kent, A. J., Till, C. Barometers behaving badly II: A critical evaluation of Cpx-only and Cpx-Liq thermobarometry in variably-hydrated arc magmas. <https://doi.org/10.31223/X59655> (2023).
80. Costa, A. Viscosity of high crystal content melts: Dependence on solid fraction. *Geophys. Res. Lett.* **32**, L22308 (2005).
81. Costa, A., Caricchi, L. & Bagdassarov, N. A model for the rheology of particle-bearing suspensions and partially molten rocks. *Geochem. Geophys. Geosyst.* **10**, Q0301 (2009).
82. Fang, X., Xu, Y. & Zhou, Z. New correlations of single-phase friction factor for turbulent pipe flow and evaluation of existing single-phase friction factor correlations. *Nuclear Eng. Design* **241**, 897–902 (2011).
83. Degruyter, W., Bachmann, O., Burgisser, A. & Manga, M. The effects of outgassing on the transition between effusive and explosive silicic eruptions. *Earth Planet Sci. Lett.* **349**, 161–170 (2012).
84. Woods, A. W. & Koyaguchi, T. Transitions between explosive and effusive eruptions of silicic magmas. *Nature* **370**, 641–644 (1994).
85. Gonnermann, H. M. & Manga, M. The fluid mechanics inside a volcano. *Ann. Rev. Fluid Mech.* **39**, 321–356 (2007).
86. Eichelberger, J. C., Carrigan, C. R., Westrich, H. R. & Price, R. H. Non-explosive silicic volcanism. *Nature* **323**, 598–602 (1986).
87. Carr, B. B., Clarke, A. B. & Vitturi, M. D. M. Volcanic conduit controls on effusive-explosive transitions and the 2010 eruption of Merapi Volcano (Indonesia). *J. Volcanol. Geotherm. Res.* **392**, 106767 (2020).
88. Jaupart, C. & Allègre, C. J. Gas content, eruption rate and instabilities of eruption regime in silicic volcanoes. *Earth Planet Sci. Lett.* **102**, 413–429 (1991).
89. Carr, B. B., Clarke, A. B. & Vitturi, M. D. M. Earthquake induced variations in extrusion rate: a numerical modeling approach to the 2006 eruption of Merapi Volcano (Indonesia). *Earth Planet Sci. Lett.* **482**, 377–387 (2018).
90. Yoshida, S. & Koyaguchi, T. A new regime of volcanic eruption due to the relative motion between liquid and gas. *J. Volcanol. Geotherm. Res.* **89**, 303–315 (1999).
91. Papale, P. Strain-induced magma fragmentation in explosive eruptions. *Nature* **397**, 425–428 (1999).
92. Roperch, P., Chauvin, A., Lara, L. E. & Moreno, H. Secular variation of the Earth's magnetic field and application to paleomagnetic dating of historical lava flows in Chile. *Phys. Earth Planet. Interiors* **242**, 65–78 (2015).

## Acknowledgements

This work was supported by the UKRI FLF project 4DVOLC (MR/V023985/1), the NERC grant DisEqm (NE/N018575/1), and the Dean's Award of the University of Manchester. We thank the Corporación Nacional Forestal-CONAF ([www.conaf.cl](http://www.conaf.cl)) and ENEL ([www.enel.cl](http://www.enel.cl)) as they provided logistic support to access outcrops. Textural analyses were carried out at the Williamson Research Centre Mineral Analysis Facility of the University of Manchester with the kind support of Lewis Huges. S.W. acknowledges funding from NERC grant NE/I02044X/1 & 2. Comments provided by Brendan McCormick and Paul Cole on an early version of the paper greatly contributed to this text. The authors are grateful with Miguel Infante, Ana Hinojosa, Víctor Hugo Sáez, Leonel Fuentes, and Curalemu cabins for their support ([www.curalemu.cl](http://www.curalemu.cl)).

## Author contributions

J.E.R., M.P., F.A., G.L.S., M.B., S.W., H.M., contributed equally on the conceptualisation of the work, on the interpretation of the results, and on the writing of the paper. G.L.S. performed the numerical simulations. C.I.S., M.A.P., J.N., A.G., L.F., and J.F. carried out analyses and data collection, and contributed on the paper writing.

## Competing interests

The authors declare no competing interests.

## Additional information

**Supplementary information** The online version contains supplementary material available at <https://doi.org/10.1038/s43247-023-00931-1>.

**Correspondence** and requests for materials should be addressed to Jorge E. Romero.

**Peer review information** *Communications Earth & Environment* thanks the anonymous reviewers for their contribution to the peer review of this work. Primary Handling Editor: Joe Aslin.

**Reprints and permission information** is available at <http://www.nature.com/reprints>

**Publisher's note** Springer Nature remains neutral with regard to jurisdictional claims in published maps and institutional affiliations.



**Open Access** This article is licensed under a Creative Commons Attribution 4.0 International License, which permits use, sharing, adaptation, distribution and reproduction in any medium or format, as long as you give appropriate credit to the original author(s) and the source, provide a link to the Creative Commons licence, and indicate if changes were made. The images or other third party material in this article are included in the article's Creative Commons licence, unless indicated otherwise in a credit line to the material. If material is not included in the article's Creative Commons licence and your intended use is not permitted by statutory regulation or exceeds the permitted use, you will need to obtain permission directly from the copyright holder. To view a copy of this licence, visit <http://creativecommons.org/licenses/by/4.0/>.

© The Author(s) 2023